Near-field microscopy by elastic light scattering from a tip

THE ROYAL
SOCIETY

Near-field microscopy by elastic
light scattering from a tip

By Fritz Keilmann[1] and Rainer Hillenbrand[2]

[1] *Abt. Molekulare Strukturbiologie and* [2] *Nano-Photonics Group,*
Max-Planck-Institut für Biochemie, 82152 Martinsried (München),
Germany (keilmann@biochem.mpg.de)

We describe ultraresolution microscopy far beyond the classical Abbe diffraction limit of one half wavelength ($\lambda/2$), and also beyond the practical limit ($ca.\,\lambda/10$) of aperture-based scanning near-field optical microscopy (SNOM). The 'apertureless' SNOM discussed here uses light scattering from a sharp tip (hence scattering-type or s-SNOM) and has no λ-related resolution limit. Rather, its resolution is approximately equal to the radius a of the probing tip (for commercial tips, $a < 20$ nm) so that 10 nm is obtained in the visible ($\lambda/60$). A resolution of $\lambda/500$ has been obtained in the mid-infrared at $\lambda = 10\,\mu$m. The advantage of infrared, terahertz and even microwave illumination is that specific excitations can be exploited to yield specific contrast, e.g. the molecular vibration offering a spectroscopic fingerprint to identify chemical composition. S-SNOM can routinely acquire simultaneous amplitude and phase images to obtain information on refractive and absorptive properties. Plasmon- or phonon-resonant materials can be highlighted by their particularly high near-field signal level. Furthermore, s-SNOM can map the characteristic optical eigenfields of small, optically resonant particles. Lastly, we describe theoretical modelling that explains and predicts s-SNOM contrast on the basis of the local dielectric function.

Keywords: near-field microscopy; apertureless optical near-field microscopy;
infrared microscopy; plasmon resonance

1. Introduction

For more than a century the classical light microscope has been serving science as one of its most fruitful instruments. It relies almost exclusively on visible light illumination. With a typical wavelength of $\lambda \approx 500$ nm, Abbe's diffraction limit allows the resolution of sample features down to $ca.\,250$ nm. A dramatic improvement of optical resolution has become possible by the invention of near-field optical microscopy, which followed the invention of scanning probe techniques initially exploiting the tunnelling of electrons (scanning tunnelling microscopy (STM)) (Binnig & Rohrer 1982), or atomic forces (atomic force microscopy (AFM)) (Binnig *et al.* 1986), that occur between a sharp scanning tip and a sample. Employing photons for tip-sensing of a sample's optical properties was independently realized by two teams (Lewis *et al.* 1984; Pohl *et al.* 1984). In their scanning near-field optical microscope (SNOM),

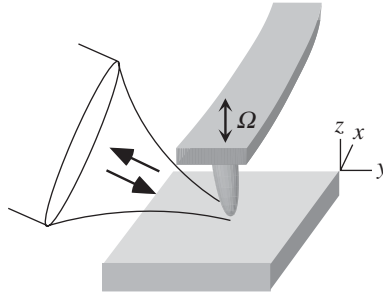One contribution of 13 to a Theme 'Nano-optics and near-field microscopy'.

Figure 1. Principle of s-SNOM. A focused light beam illuminates the tip region of an AFM, where a sample is approached and scanned to produce a topographic image. By recording the scattered light, here in the backwards direction, an optical image is simultaneously generated. The tip oscillates at the cantilever's mechanical resonance frequency Ω (tapping mode) with the important consequence that the near-field optical signal becomes modulated at harmonics $n\Omega$, allowing an electronic filtering against otherwise overwhelming background scattering coming from the shaft and cantilever.

a submicrometric, metallic aperture with diameter d confines the 'near-field' light emanating from or entering the tip. In principle, d could be made very small to achieve very high resolution. In practice, however, the common funnel-shaped geometry of a metallized, tapered glass fibre (Betzig *et al.* 1991) causes the well-known waveguide cut-off effect (Jackson 1975), so light propagation becomes evanescent when the diameter is below the critical cut-off diameter, given by $d_c = 0.6\lambda/n$. The consequence is a drastic, λ-*dependent* loss (Knoll & Keilmann 1999a) which practically limits the achievable resolution—depending on how small a signal power can be detected—to minimal apertures, $d \approx \lambda/10$, so that a resolution of *ca.* 50 nm is obtained in the visible (Hecht *et al.* 2000). For mid-infrared illumination, the resolution of SNOM is 1 μm at best, which is not really an interesting value for applications in the nanosciences.

An alternative SNOM principle with much better resolution potential is to use a small scatterer instead of a small aperture (O'Keefe 1956; Wessel 1985; Wickramasinghe & Williams 1990; Specht *et al.* 1992; Inouye & Kawata 1994). This rests on the fact that an illuminated particle can exhibit enhanced optical fields in its neighbourhood. Such near fields are modified by the presence of a sample. As a consequence of this near-field interaction, the scattered light measured in the far field carries information on the sample's local optical properties. This near-field scattering is the basis of what has been named s-SNOM: scattering-type scanning near-field optical microscopy. In practice, the elongated metallized tip of an AFM serves as a scatterer (figure 1), and it is the radius of curvature a at its apex that determines both the mechanical and the optical resolution.

The highly concentrated near fields at a metallic tip apex also give rise to enhanced Raman scattering (tip-enhanced Raman scattering), which can be exploited for chemical microscopy (Stöckle *et al.* 2000; Hayazawa *et al.* 2002; Hartschuh *et al.* 2003).

The paper is organized as follows. First, we introduce the principle of s-SNOM, its components and configurations. Then we consider the theory, describing in detail a point–dipole model which can qualitatively explain the majority of all experimental findings. The following section gives experimental details, with an emphasis on how disturbing background scattering can be suppressed, and how high-resolution ampli-

tude and phase contrast is made possible by interferometric detection. The results achieved are discussed for their significance in demonstrating the optical contrast and resolution obtainable with s-SNOM. A special section is devoted to optical resonance, which means the possibility of having an extremely high signal in s-SNOM images from samples (or tips) with negative dielectric constant. Going beyond probing a sample's local optical property, we describe an application of s-SNOM to the analysis of the patterns of the optical eigenfield surrounding small sample structures that are resonantly excited. Lastly, we mention areas of application of s-SNOM in the nanosciences such as the mapping of subsurface charge carriers in Si, and the analysis of nanocomposite dielectrics.

2. Principle of s-SNOM

A basic experimental set-up is illustrated in figure 1. Here an AFM is used as a base instrument (STM is an alternative (Bragas & Martinez 2000)) to scan a sample in close proximity to a cantilevered tip. This generates, first of all, a topographic image of the sample. The tip is illuminated by a focused visible or infrared beam so that, secondly, the scattered light is recorded by a detector to give an optical image of the sample. In principle, input and output directions could be freely chosen. Backscattering as shown in figure 1 has the practical advantage that only one focusing objective has to be adjusted.

Typically, the tip has a radius of curvature of $a \approx 20$ nm. The probing region is the gap between the tip apex and the sample, a space much smaller than the applied focus spot. Due to the AFM tapping mode, this gap is sinusoidally varied between 0 and, for example, 40 nm. A strong modulation of the near-field scattering results, whereas, advantageously, the 'background' scattering from portions of tip and sample outside the probing region is barely modulated, and therefore can be electronically eliminated from the detector signal.

An early implementation of s-SNOM (Zenhausern *et al.* 1995) used a dielectric tip which has a principal limitation to the fraction of the illuminating power that can effectively couple to the probing gap. In contrast, highly conductive tip materials can greatly increase this fraction, as can be extrapolated from the effective functioning of metal antennas in radio and microwave engineering (Jackson 1975). Antenna efficiencies have been experimentally analysed up to the mid-infrared region (Wang 1976; Völcker *et al.* 1994), and one can hope that tailored tips (Krug *et al.* 2002) can in future strongly increase the coupling of illuminating light into an enhanced probing near field, and also back out to a far-field detector.

For highly conductive metallic shafts the antenna theory predicts that optical currents can be excited much more strongly in directions parallel rather than perpendicular to the shaft axis (Jackson 1975). This antenna effect should make itself felt by forcing the probing near field to be fully z-polarized. We have tested this prediction in an experiment with an Au-coated tip illuminated by the mid-infrared beam from a CO_2 laser, the polarization of which could be rotated while the light scattered to the detector did not pass through a polarizing element (Knoll & Keilmann 1999*b*). The result shown in figure 2 illustrates clearly that the optical image loses contrast when the input polarization has no component along the shaft axis. This effect indicates that the shaft acts as an antenna, or, more precisely, that it can enhance the probing near field in the z-direction.
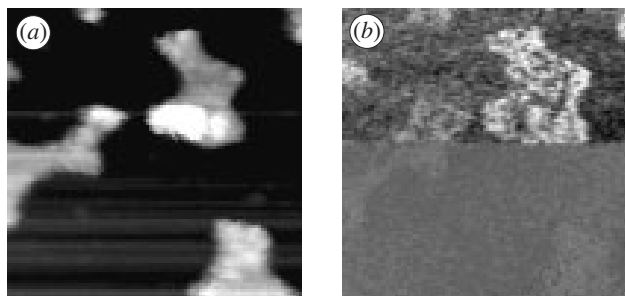
Figure 2. (*a*) Topography and (*b*) infrared near-field image of a test sample consisting of 20 nm high Au islands on Si (image area 1 μm^2). Halfway through the image scan, the polarization was flipped from *z–y* (upper part) to *x* (lower part), to investigate the antenna function of the tip shaft.

Various, mostly home-built, s-SNOMs have been reported in the literature (Specht *et al.* 1992; Inouye & Kawata 1994; Zenhausern *et al.* 1995; Lahrech *et al.* 1996; Knoll & Keilmann 1999*b*; Adam *et al.* 2000; Aigouy *et al.* 2000; Bragas & Martinez 2000; Hillenbrand & Keilmann 2000; Sasaki & Sasaki 2000; Akhremitchev *et al.* 2001; Hayazawa *et al.* 2002). We have built two AFM-based s-SNOMs to operate in tapping mode with visible (Hillenbrand & Keilmann 2000) or mid-infrared illumination (Taubner *et al.* 2003). Both use Pt-coated cantilevered tips available commercially from Nanosensors (www.nanosensors.com) or MikroMasch (www.spmtips.com). These instruments implement interferometric signal detection (Bridger & McGill 1999; Azoulay *et al.* 2000; Sasaki & Sasaki 2000), which allows us to measure both the amplitude and the phase of the near-field scattering interaction, especially enabling near-field phase contrast imaging (Hillenbrand & Keilmann 2000, 2001, 2003). Two interferometer versions have been realized, a Michelson-type with homodyne detection (Hillenbrand *et al.* 2002; Taubner *et al.* 2003), and a Mach–Zehnder-type with heterodyne detection (Hillenbrand & Keilmann 2000; Hillenbrand 2001; Hillenbrand *et al.* 2001), as will be detailed below (see figure 5).

3. Theory of s-SNOM

Two observables are of prime practical importance in s-SNOM: the *absolute* scattering efficiency which determines the observable signal power, and the contrast or *relative* signal change which results when probing different materials. A theoretical treatment of the scattering of a realistic, elongated tip is complicated (Porto *et al.* 2000) and has not been tried by us. The shaft's shape and length dominate the *absolute* scattering efficiency as can be expected from antenna theory. For qualitatively calculating the *relative* scattering when probing different materials, however, we have found a solution by simplifying the geometry (Knoll 1999; Knoll & Keilmann 1999*c*; Hillenbrand & Keilmann 2000; Hillenbrand *et al.* 2001). We assume that the near-field contrast or, generally, the way a sample influences the near field between tip and sample does not primarily depend on the existence of the tip's shaft. Rather, it suffices to approximate the elongated tip by the sphere which can be inscribed in its apex.

Accordingly, we assume that the probe is a polarizable sphere with dielectric value ε_t, radius $a \ll \lambda$, and polarizability:

$$\alpha = 4\pi a^3 \frac{\varepsilon_t - 1}{\varepsilon_t + 2}. \tag{3.1}$$

We further assume that the dipole induced in this sphere by an incident field E_i can only point in the z-direction. This polarization direction is suggested by the antenna action of the tip's shaft leading to an enhanced near field. The sample, which fills the half-space $z < 0$ with dielectric value ε_s, is assumed to be polarizable only indirectly by the sphere's dipolar field, but not directly by the incident field, because the tip's enhanced near field exceeds the incident field. The configuration of a small sphere next to a flat sample has been theoretically treated before in the context of surface-enhanced Raman scattering (SERS) (Ruppin 1982; Aravind & Metiu 1983). To simplify the calculation of the polarization induced in the sample, we then replace the sphere by a point dipole of equal strength and direction, located in the sphere's centre. In the electrostatic limit (no retardation considered) the near field between tip dipole and sample can be found by considering a 'mirror' point dipole inside the sample whose direction is parallel to the tip dipole, with polarizability $\alpha\beta$, where

$$\beta = \frac{\varepsilon_s - 1}{\varepsilon_s + 1} \tag{3.2}$$

is the dielectric surface response function of the sample. The mirror dipole's field, decreasing with the third power of distance, interacts with the tip dipole. Solving the system of electrostatic equations that describes the multiple interaction between tip and mirror dipoles yields an effective polarizability of the coupled tip–sample system which fully expresses the influence of the sample,

$$\alpha_{\text{eff}} = \frac{\alpha(1 + \beta)}{1 - \alpha\beta/(16\pi(a + z)^3)}. \tag{3.3}$$

Since, generally, the scattered field $E_s \propto \alpha E_i$ from a point dipole is directly proportional to its polarizability α (Bohren & Huffmann 1983), equation (3.3) is a centrally important result for s-SNOM, as it contains all that is necessary to predict relative contrasts observable in s-SNOM. First, we note that ε, β and α are, in general, complex-valued quantities. Thus the scattering $E_s \propto \alpha_{\text{eff}} E_i$ from the coupled dipole system is also, in general, complex valued, $\alpha_{\text{eff}} = se^{i\varphi}$, characterized by a relative amplitude s and a generally non-zero phase shift φ between the incident and the scattered light. To measure both these quantities simultaneously motivates our use of interferometric detection.

Especially, equation (3.3) reveals that a sample affects the s-SNOM signal only through its dielectric value ε_s taken at the wavelength of illumination. This provides the basis to view s-SNOM as a nanospectroscopic tool, to measure the local dielectric function for identifying nanosystems according to their known (far-field) optical and infrared dielectric spectra. We further observe that the probing sphere also enters equation (3.3) by its dielectric value ε_t, besides its radius and its distance z from the sample. Since both ε_t and z are constant during the imaging process, the optical image contrast is determined only by the sample's local dielectric value ε_s.

Before giving examples of material contrast we discuss another consequence of equation (3.3), the dependence $\alpha_{\text{eff}}(z)$, which is, as we shall see, of prime importance for the practical, background-free performance of s-SNOM. As an example, we
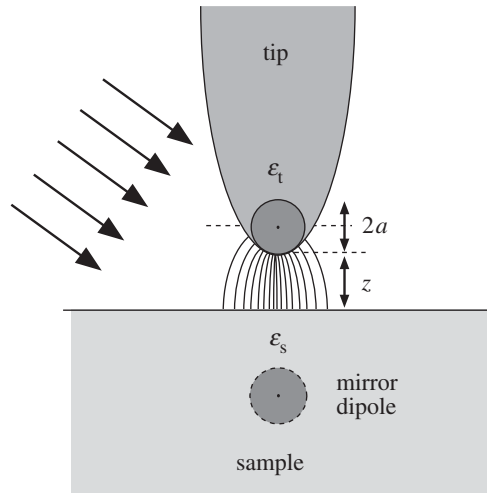
Figure 3. Modelling the near-field interaction in s-SNOM. The replacement of the probing tip by a point dipole allows to predict how the scattered light depends on (i) the distance z between tip and sample, and (ii) on the complex dielectric value ε_s of the sample.
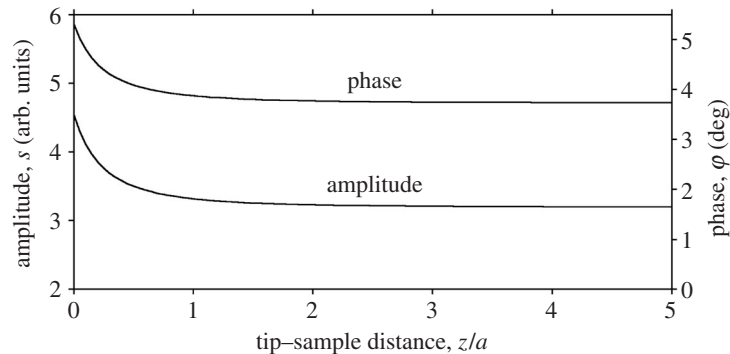

Figure 4. Calculated near-field scattering amplitude s and phase φ versus the distance z between the tip sphere and the sample.

assume the sample to be Si with real dielectric value $\varepsilon_s = 15$, and the tip sphere to be Au, with radius $a = 10$ nm and dielectric value $\varepsilon_t = -10 + 2i$ (corresponding to $\lambda = 633$ nm). As displayed in figure 4 equation (3.3) predicts a constant scattering at relatively large distance $z \gg 2a$ (note the neglect of retardation restricts the applicability of this modelling to $z \ll \lambda$). At very small distances, $z < a$, however, both the scattering amplitude and the scattering phase increase sharply. Such a nonlinear rise occurs with any combination of dielectric values and can be taken as signature of the near-field interaction. It is interesting that the z-range of near-field interaction is of the same order as the lateral width of the confined near field, both being of the order a, the sphere's radius (Taubner *et al.* 2003). A multipolar theory that includes retardation has recently given a similar result (Porto *et al.* 2003). In the following, we keep to the non-retarded, dipolar approximation because it allows the simple solution equation (3.3) from which direct conclusions of practical significance can be derived.
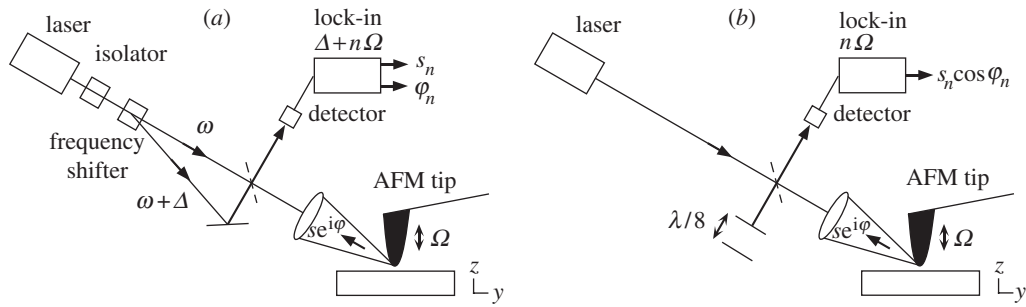
Figure 5. Sketches of optical layouts for interferometric s-SNOM. (*a*) Heterodyne system where the frequency in the reference arm of a Mach–Zehnder interferometer is offset by frequency Δ (80 MHz in Hillenbrand & Keilmann (2000)). (*b*) Homodyne system where the phase of the reference beam in a Michelson interferometer is alternated between $\psi = 0$ and $90°$ by mechanical mirror translation.

4. Elimination of background-scattering contributions from the detector signal

The nonlinear dependence $\alpha_{\mathrm{eff}}(z)$ seen in figure 4 is the basis of a signal processing technique essential to the solution of the experimental difficulty of how to deal with the massive, unwanted 'background' scattering which generally dominates the detected signal. The focused laser beam illuminates a greater part of the tip shaft which typically extends $10\,\mu$m from the cantilever, and also the sample. Because there is no special attempt to match the incoming light to the largely unknown antenna property of the tip–sample configuration, only a small portion of the incident light can be assumed to reach the gap region and to contribute to the probing near field. Most of the intercepted light is scattered as unwanted background, without contributing to the near-field interaction. The early suggestion (Wickramasinghe & Williams 1990) of z-modulation and electronically filtering the detector signal at the tapping frequency Ω is not generally sufficient to suppress the background. Rather, a full elimination requires demodulating the detector signal at the second or higher harmonic of Ω (Wurtz *et al.* 1998; Hillenbrand & Keilmann 2000; Knoll & Keilmann 2000*a*; Labardi *et al.* 2000; Hillenbrand *et al.* 2001). The key is that the tapping motion, with an amplitude of typically $\Delta z \approx a \approx 20\,$nm, modulates the near-field scattering much more strongly than the background scattering, inducing harmonics $n\Omega$ (where $n = 2, 3, \dots$) by the nonlinear dependence $\alpha_{\mathrm{eff}}(z)$ seen in figure 4. Before we describe experimental details and results (figures 6 and 7), we note here that the successful elimination of background scattering by harmonic-demodulation processing has, however, a price to be paid. The s-SNOM image no longer measures the near-field scattering $\alpha_{\mathrm{eff}} = s\mathrm{e}^{\mathrm{i}\varphi}$ directly. Rather, it maps the complex quantity $s_n\mathrm{e}^{\mathrm{i}\varphi_n}$ derived from it. To see this, consider the sinusoidal tapping motion between z and $z + 2\Delta z$ at frequency Ω, which induces a time-periodic scattering $\alpha_{\mathrm{eff}}(t)$. Because of the nonlinear dependence $\alpha_{\mathrm{eff}}(z)$ the scattering signal is modulated at harmonics of Ω. In general, the time course can be described by a Fourier series with s_n and φ_n being Fourier coefficients. For the case of small modulation amplitude, $\Delta z \ll a$, the Fourier coefficients are proportional to the nth z-derivative of $\alpha_{\mathrm{eff}}(z)$ (Hillenbrand & Keilmann 2000; Hillenbrand *et al.* 2001).
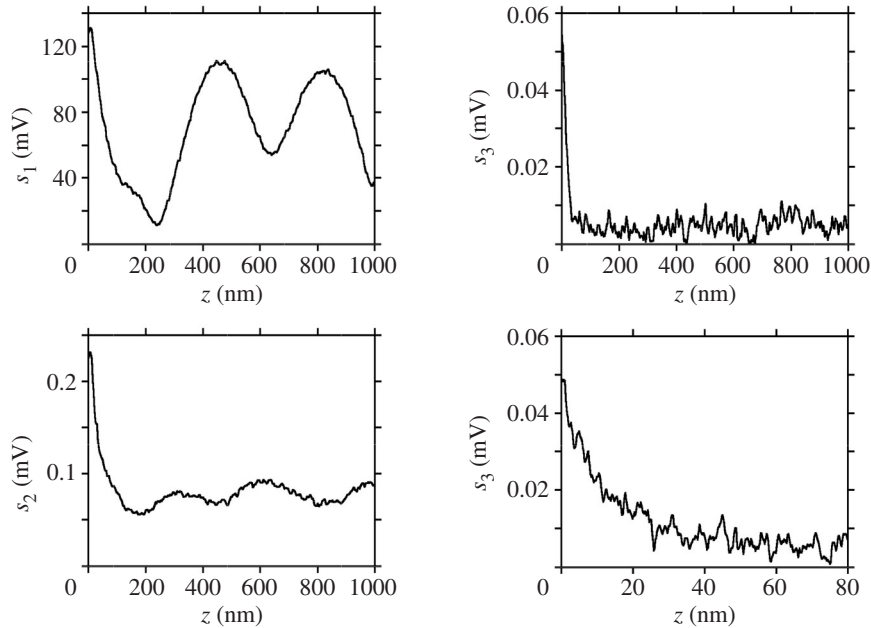
Figure 6. Comparison of experimental s-SNOM amplitude versus distance z between Pt tip and Si sample, for $n = 1$–3 demodulation orders (tip radius $a \approx 20$ nm, tapping amplitude $\Delta z \approx 20$ nm, wavelength $\lambda = 633$ nm). Choice of a high n eliminates the background, and also steepens the near-field response.
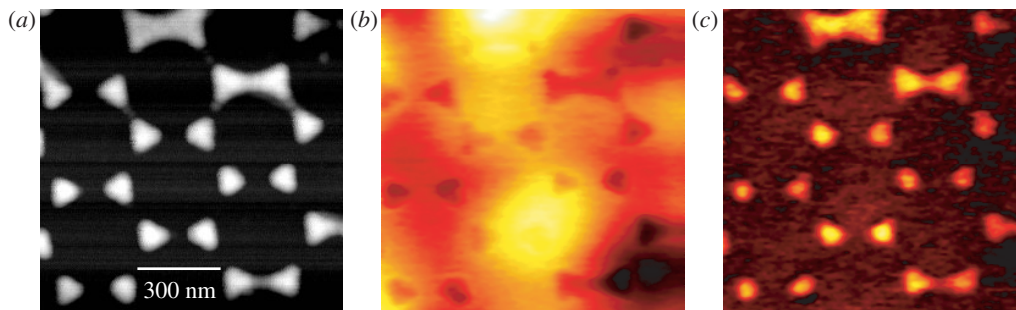

Figure 7. Experimental s-SNOM images of 20 nm high Au islands on Si. (a) Topography, (b) optical amplitude s_1 showing residual background scattering, and (c) optical amplitude s_3 showing pure near-field response.

5. Experimental realization of s-SNOM

Figure 5 shows our (a) visible and (b) infrared microscopes. The former set-up described in Hillenbrand & Keilmann (2000) and Hillenbrand *et al.* (2000a) uses an HeNe laser beam of *ca.* 1 mW power that is focused to the tip apex by an aspheric lens. Backscattered light is collected by the same lens and detected by a heterodyne interferometer. Here the reference beam is frequency-shifted by $\Delta = 80$ MHz. The detector measures the power

$$I = I_{\mathrm{ref}} + I_{\mathrm{s}} + 2\sqrt{I_{\mathrm{ref}}I_{\mathrm{s}}}\cos(\Delta t + \varphi)$$

generated by the interference of the strong reference beam and the weak, backscattered light from the probing tip. To measure both amplitude and phase the detector signal is processed in a high-frequency lock-in amplifier (Mod. 844 Stanford Research Systems) operating not at Δ but at the sum frequency $\Delta + n\Omega$ (where n designates the order of harmonic signal demodulation) (Hillenbrand & Keilmann 2000; Hillenbrand 2001; Hillenbrand *et al.* 2001). This side-band filtering allows us to suppress, in one instrument, any constant power as well as the tip's background scattering, which beats with the reference to yield a modulation at Δ. Conversely, demodulation at $\Delta + n\Omega$ selects scattered light that is influenced by the mechanical modulation of the near-field interaction. The lock-in amplifier produces two output signals simultaneously, one proportional to the amplitude, the other proportional to the phase of the detector modulation at frequency $\Delta + n\Omega$. This is very convenient because, at sufficiently large n, the amplitude output signal is directly proportional to s_n and the output phase to φ_n measuring the pure near-field response. Because of interference with the reference beam, the near-field signal power level appears amplified by a factor twice the square root of the ratio between the reference and near-field light powers, which can be large. This so-called heterodyne gain is a convenient byproduct of our scheme, as it helps to optimize the signal/noise ratio (Taubner *et al.* 2003).

Background reduction by harmonic demodulation becomes directly visible in approach curves such as those shown in figure 6. At demodulation order $n = 1$, standing wave features that extend far beyond the near-field interaction zone, $z < a$, dominate. These result from interference of different background contributions and may mask the expected near-field increase at $z < a$ (see figure 4). With increasing n, however, the near-field contribution becomes clearly visible and even steepens, whereas the standing wave features are suppressed and are even lost in noise at $n = 3$. Not visible in figure 6, the possibility of an artefact arises once the tip periodically touches the sample, because then the tapping motion can become non-sinusoidally distorted, which means that harmonics $n\Omega$ are excited in the mechanical motion. This effect has been studied and found to be dependent on the sample and on some tapping characteristics such as, for example, whether the mechanical interaction is attractive or repulsive, and the tapping amplitude Δz (Hillenbrand *et al.* 2000*b*; Stark *et al.* 2002). We found that with small $\Delta z < 50$ nm, and large setpoint $\Delta z/\Delta z_{\text{free}} > 0.9$, mechanical harmonics are negligibly small. To fully exclude an influence on the optical signal a routine control is recommended, taking approach curves such as those in figure 6 at the beginning of an s-SNOM imaging session.

We demonstrate near-field optical mapping using higher-harmonic demodulation by imaging a common test sample (figure 7). Its nanoscale structure is made by evaporating metal on a substrate which is covered by a monolayer of polystyrene (PS) microspheres. These are subsequently dissolved by dichloromethane and washed away (Fischer 1998). Here we use a Si substrate with 20 nm high Au islands, as documented by the topographic image. Furthermore, figure 7 shows two optical near-field images taken at the fundamental and the third harmonic demodulation orders, respectively. The former image (figure 7*b*) displays—due to the influence of considerable background scattering—large patches which do not correspond to real sample structures. Furthermore, the islands appear in reversed, dark contrast. We explain the large patches by interference between various components of background-scattered light, and the reversed contrast of the islands by a negative interference between the near-field-scattered light and the background-scattered light. The latter explanation

can be experimentally tested by slight adjustments of the illuminating laser focus. Indeed small variations suffice to reverse the apparent near-field contrast, evidently by changing the background's phase (Knoll & Keilmann 1999*c*, 2000*a*). The optical image taken at third harmonic demodulation order (figure 7*c*), however, displays the Au islands with uniform brightness and in the positive contrast expected from calculations (see figure 8), independently of slight adjustments of the illuminating laser focus.

In our infrared set-up we use a CO_2 laser for tip illumination, common to both groups which pioneered the mid-infrared s-SNOM (Lahrech *et al*. 1996; Knoll & Keilmann 1999*b,c*). We have exploited the fact that our laser is step-tunable in the region between 9.2 and 11.2 µm to demonstrate near-field nanospectroscopy using infrared vibrational (Knoll & Keilmann 1999*c*; Hillenbrand *et al*. 2002) or electronic (Knoll & Keilmann 2000*b*) resonances for the first time.

The incident beam is attenuated to *ca.* 10 mW (LASNIX, www.lasnix.com) and focused to the tip apex by a Cassegrain mirror objective with a numerical aperture of 0.55 (Ealing, www.cohr.com). A focal spot with diameter as small as 15 µm has been experimentally demonstrated (Knoll & Keilmann 2000*a*). The polarization is set to maximize the component along the tip shaft, in order to optimize the antenna coupling. Orthogonal polarization was experimentally shown to lead to loss of contrast (figure 2) (Knoll & Keilmann 1999*b*).

The infrared s-SNOM work already mentioned and that of a third laboratory (Akhremitchev *et al*. 2001) used simple direct detection of the scattered infrared light by an HgCdTe detector. While there is no external reference beam, we have observed that this detection is nonetheless of interferometric type (Knoll 1999; Knoll & Keilmann 1999*c*, 2000*a*). The reason is the omnipresent background scattering which constitutes a reference beam that superimposes coherently with the near-field scattered light. Because there is no frequency offset, the detection system is therefore, strictly speaking, a homodyne receiver. As mentioned above the phase of this interferometer can be adjusted by adjusting the focus of the incident beam (Knoll & Keilmann 2000*a*).

Recently, the infrared s-SNOM has been improved qualitatively (Taubner *et al*. 2003) by introducing interferometric detection with an external reference beam which is, of course, much more controllable. This is achieved by splitting the incoming collimated CO_2 laser beam to generate a reference beam which is reflected from a piezo-electrically movable plane mirror. Thus we form a Michelson interferometer which has the scattering tip at the end of the other side arm. The reference is much stronger than the background-scattered light, and we therefore now have a homodyne receiver in which the reference phase can be conveniently set by moving the Michelson mirror. In practice, we continuously alternate between recordings using two mirror positions. The first position is obtained at the beginning of an experiment, by maximizing the lock-in amplified detector signal (usually second or third harmonic demodulation). This position corresponds to positive interference between near-field scattered light and the reference beam. The second position is obtained by moving a distance of $\lambda/8$, which changes the reference phase by $\psi = 90°$. Simple computing yields an unambiguous pair of values, the amplitude and the phase of near-field scattering, for each pixel of the scanned image. Each scan line is repeated once, and the mirror position is switched after each scan. Typically, it takes 1 s to completely determine
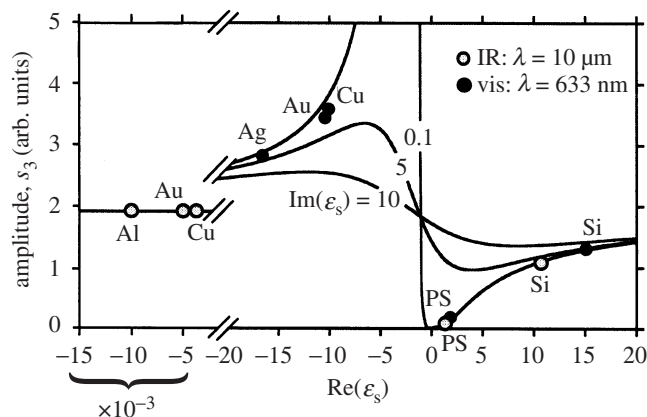
Figure 8. Predicted s-SNOM amplitude s_3 of various sample materials at two different illumination wavelengths, on a general graph where the abscissa is the real part of the sample's dielectric function, and the imaginary part serves as a parameter (Pt tip with $a = 20$ nm, $\Delta z = 20$ nm).

one 256 pixel line. With this method, the infrared s-SNOM produces simultaneous near-field phase-contrast images and near-field amplitude-contrast images.

6. Contrast and resolution in s-SNOM images

We recall from equation (3.3) that the observable scattering $se^{i\varphi}$ (and consequently also $s_n e^{i\varphi_n}$) depends on the dielectric values of both the tip and the sample. This means that the choice of a tip material can influence what is seen in s-SNOM. For example, when using an Au tip in the visible region, the s-SNOM amplitude and phase varies with frequency due to the strong variation of ε_t of Au, as we have calculated (Hillenbrand & Keilmann 2000, fig. 2). While such influences can be straightforwardly corrected for (equation (3.3)), clearly a tip material which does not itself show a strong dispersion within the studied spectral region is preferred when measuring a sample's near-field spectrum. For a fixed-frequency application, the choice of a resonant tip material (see below) could greatly enhance the amplitude and/or phase sensitivity of the s-SNOM.

In the following we discuss how the dielectric value ε_s of the sample determines the near-field signal at contact, $z = 0$. We use equation (3.3) to predict the relative contrast between various sample materials (Taubner *et al.* 2003), thereby assuming a sinusoidal tapping motion between $z = 0$ and $z = 40$ nm, and taking account of the harmonic signal demodulation in s-SNOM signal processing, here at 3Ω. We assume that the sphere material is Pt, for the practical reason that AFM tips coated with this metal are both durable and readily available. As seen in figure 8, the theory thus predicts that typical, low-refractive-index dielectrics such as PS produce a very weak near-field scattering s_3. It might, however, increase when such materials were absorbing. Much stronger near-field scattering is predicted for materials with large dielectric value $\mathrm{Re}(\varepsilon_s)$. Interestingly, this remains true independently of whether $\mathrm{Re}(\varepsilon_s)$ has positive or negative sign, and also independently of whether the imaginary part is small or large. The highest s-SNOM amplitudes s_n are predicted for materials with negative $\mathrm{Re}(\varepsilon_s) \approx -1$ and very small $\mathrm{Im}(\varepsilon_s)$, which we call polariton-resonant materials as discussed below.
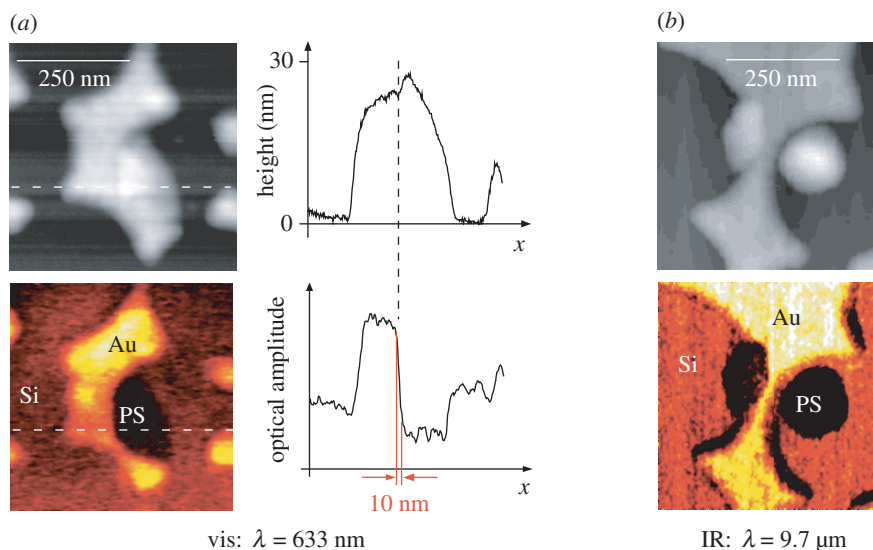
Figure 9. Experimental s-SNOM images obtained with a three-component test sample. Use of two different wavelengths ((*a*) visible and (*b*) mid-infrared) testifies that (i) resolution is independent of wavelength (10 nm from line trace through visible image), and (ii), that image contrast is independent of wavelength, confirming predictions of the theoretical model.
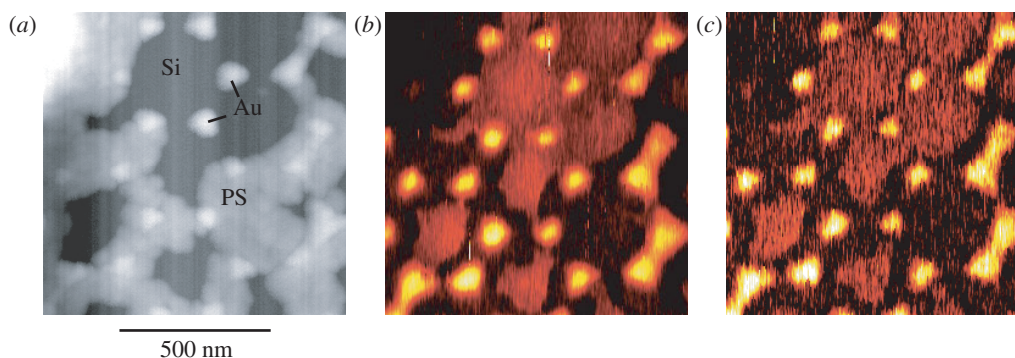

Figure 10. Experimental s-SNOM images obtained with a three-component test sample ($\lambda = 633$ nm). (*a*) Topography, (*b*), (*c*) s-SNOM amplitude taken at demodulation orders of $n = 3$ and $n = 4$, respectively.

From the results in figure 8 we predict that s-SNOM images will readily allow us to distinguish categorical material classes by amplitude contrast alone: polariton-resonant materials give exceptionally large signals, metals large signals, semiconductors medium signals, and low-index dielectrics low signals (Hillenbrand & Keilmann 2002). Different metals will appear indistinguishable if probed with mid-infrared illumination, but should appear with marked difference in contrast when probed in the visible (Koglin *et al.* 1997).

We have used a test sample composed of three different materials for determining the relative contrasts and the obtainable spatial resolution (figure 9). We have studied this sample both in the visible and in the infrared s-SNOM, with the aim of comparing the results obtained at widely different wavelengths (Taubner *et al.* 2003).
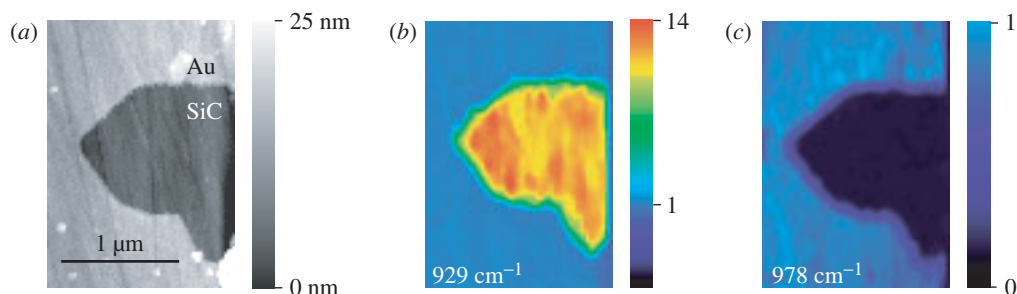
Figure 11. Experimental s-SNOM images obtained with a partly Au-covered SiC sample. (a) Topography, (b), (c) s-SNOM amplitude s_2 taken at two different mid-infrared illumination frequencies which are on and off the tip-induced, phonon-polariton near-field resonance, respectively.

The sample is prepared as in figure 7 but without complete dissolution of the PS microspheres. Irregularly shaped PS remainders are found in many places. The topography alone does not suffice to distinguish between Au and PS, and the near-field images provide the needed extra information. In good agreement with our model calculation (figure 8) the Au islands appear brighter than Si, which in turn appears brighter than PS. The near-field signal on PS is in the noise level for both wavelengths. When we compare the amplitude contrasts between Au and Si quantitatively, we find for $n = 3$ a ratio of about 3:1 at a wavelength of 633 nm and 1.7:1 at a wavelength of 10 µm (averaging over several images). These values are in close agreement with the predicted ratios of 2.5:1 and 1.8:1, respectively, so the ability of s-SNOM to distinguish material classes is excellently confirmed. In addition, this agreement can be taken as verification of the theoretical model.

Figure 10 shows further images from this test sample. Here we demonstrate the influence of the demodulation order n on the three-component image contrasts. Evidently, there is no qualitative difference between the images obtained at $n = 3$ (figure 10b) and $n = 4$ (figure 10c). This indicates a general robustness we have often observed of the s-SNOM image against changes of parameters of the background elimination procedure.

As to the spatial resolution, we observe in the visible near-field image (left-hand part of figure 9a) that the bright-to-dark transition between Au and PS materials occurs within 10 nm (see line scans). Since there is a negligible height step at this boundary, our measurement excludes the possibility of a height-induced artefact, and proves that the near-field optical resolution is indeed 10 nm. The mid-infrared image shows approximately the same resolution of *ca.* 20 nm, $\lambda/500$. Here the fact that the PS particles are somewhat higher makes an exact determination less stringent. These images can be taken as a direct proof that the s-SNOM's resolution does not depend on the illuminating wavelength.

7. Near-field-induced polariton resonance

We have demonstrated in two cases (Knoll & Keilmann 2000b; Hillenbrand *et al.* 2002) that the near-field-scattering amplitude when probing a polaritonic sample material can be enormously enhanced. By polaritonic material we mean a material which interacts so strongly with light that its dielectric value becomes distinctly

negative. At the frequency where $\mathrm{Re}(\varepsilon_s) = -1$ our model equation (3.3) shows that, because the dielectric surface response function β (equation (3.2)) becomes large, the scattering also becomes large. As figure 8 illustrates, the amplitude can indeed become very high at this dielectric value, much higher than that of the noble metals, especially if the damping expressed by $\mathrm{Im}(\varepsilon_s)$ is small. This 'tip-induced near-field resonance' is accompanied by strong phase changes, as evaluated in the prediction shown in fig. 3 of Knoll & Keilmann (2000*b*).

The tip-induced near-field resonance we have studied in greater detail (Hillenbrand *et al.* 2002) is that of SiC caused by the phonon-polariton in the mid-infrared, i.e. by the interaction of light with the fundamental lattice vibration. The s-SNOM equipped with a (non-resonant) metal tip is used to determine the resonance spectrum peaking at a wavelength of 10.6 µm. The response is determined relative to that of a 10 nm Au film partly covering the SiC crystal. At resonant illumination the near-field amplitude of SiC exceeds that of Au by one order of magnitude (figure 11). The resonance is extremely narrow (1% full-width half-maximum), more than an order of magnitude sharper than the far-field 'Reststrahlen' reflectivity spectrum of SiC. This spectral narrowing promises a sensitive spectral distinction of otherwise overlapping infrared signatures of polar dielectrics. Thus it can be predicted that near-field microscopy enables a much better material discrimination ('chemical microscopy') than is possible with the common, diffraction-limited Fourier transform infrared microscope. Especially, one can hope that the narrowing will enable us to discriminate not only between chemically different species, but also between crystalline subtypes or physically different phases of chemically homogeneous nanostructures (Hillenbrand *et al.* 2002). The very strong scattering should make any polaritonic material exceptionally visible in the ultraresolution microscopy of nanoscale composite structures. This material-selective highlighting should prove widely useful in the nanosciences.

8. Nanoscale coherent imaging of optical eigenfield patterns

In small metal particles, light can resonantly excite collective oscillation modes of conduction electrons. Such plasmon-resonant particles have long been known for their strong scattering and enhanced near field close to their surface (Kreibig & Vollmer 1995). Because of the enormous potential for the application of plasmon-resonant particles—for example, in SERS for single-molecule detection (Kneipp *et al.* 1997) or to guiding light in nanoscale dimensions (Salerno *et al.* 2002)—a method for studying the near-field distributions is of utmost importance. Krenn *et al.* (1999) and Adam *et al.* (2000) have already demonstrated that the particle's near fields can be imaged by near-field optical microscopy using fibre and scattering probes, respectively. With our visible s-SNOM we have shown that eigenfields of plasmon-resonant particles can be mapped not only at nanoscale resolution but even in both their amplitude and phase distributions (Hillenbrand & Keilmann 2001, 2003).

The possibility of imaging the eigenfield E_p of a resonant particle rests on the fact that the particle can be directly excited by the illuminating field E_i (figure 12*a*). We assume that this eigenfield acts as an additional illumination of the tip. The tip is thus excited by a sum of fields, $E_{loc} = E_i + E_p$, and the measured field is $E_s \propto \alpha_{eff} E_{loc}$. After this model, a genuine mapping of the eigenfield E_p is directly possible in the strong-enhancement limit, $E_p \gg E_i$. We further assume that only the z-oriented component of E_p is detectable, since other components couple only weakly
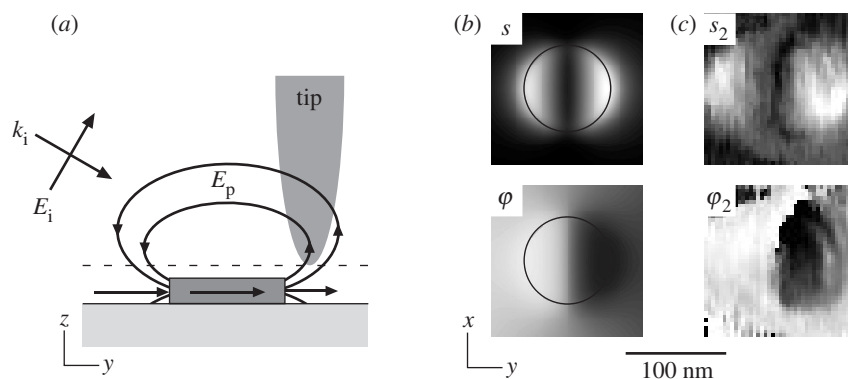
Figure 12. Dipolar surface-plasmon-polariton oscillation field pattern of an Au disc (91 nm diameter, 20 nm high) on glass induced at a wavelength of 633 nm. (a) Schematic side view of the incident plane wave E_i and of the particle's eigenfield E_p. (b) Top view of near-field amplitude (upper row) and phase (lower row) for the field's z-component, obtained by exact electrodynamic calculation of the total field 10 nm above the disc as marked by the dashed line in (a). (c) Experimental s-SNOM amplitude E_2 and phase φ_2 images using a carbon nanotube tip as near-field-scattering optical probe.

to the shaft's antenna, which is, on the other hand, necessary for efficient emission. Near-field phase contrast in eigenfield imaging arises from both an intrinsic phase shift between E_p and E_i, and from the geometric separation between particle and tip (Hillenbrand & Keilmann 2001).

Recently, we measured the eigenfield patterns of well-defined Au nanodiscs on glass, tailored to be in optical resonance with $\lambda = 633$ nm used to illuminate our s-SNOM (91 nm diameter, 20 nm height). As illustrated in figure 12a we expect antiphase optical fields near two pole regions due to the designed, dipolar oscillation. To minimize a possible perturbation of E_p by the probing tip we used a carbon nano-tube tip (Hillenbrand & Keilmann 2003). We obtained good qualitative agreement between the measured amplitude and phase images (figure 12c) taken at demodulation order $n = 2$, and the exact electrodynamic field calculation (figure 12b), which does not include any influence of the tip on the particle's eigenfield. This demonstrates that both the presence of the probing carbon nanotube and the harmonic demodulation procedure do not perturb the eigenfield pattern significantly.

Using bare Si tips, we could furthermore observe (Hillenbrand & Keilmann 2001) highly confined (less than 10 nm) near fields in narrow gaps between resonant particles. Such fields may be basic for colossally enhanced SERS (Kneipp *et al*. 1997; Xu *et al*. 1999), to provide a mechanism for the observation of single molecules. Strong gap fields seem an ideal geometry for doing nonlinear spectroscopy of nanoscale objects and for other high-field physics experiments. They could possibly be mapped in nanometric resolution by s-SNOM equipped with a single-wall carbon nanotube probe tip.

9. General application potential of s-SNOM

The s-SNOM has so many excellent capabilities that it should have a bright future in the nanosciences. The presently achieved spatial resolution of less than 20 nm could improve even more if sharper tips become available, possibly by as much as

an order of magnitude. Various applications in nanophysics and nanotechnology can be foreseen that use, for example, the ability to discriminate between a metal, a semiconductor and a low-refracting dielectric. The s-SNOM when used in the visible should discriminate well between different metals (figure 8). The phase-sensitive mapping of nanoscale field distributions could be valuable in plasmon photonics, to analyse the coherent control of plasmon-polariton excitation. A special advantage over any other form of light microscopy is that the s-SNOM can work with mid-infrared and probably also far-infrared illumination. In fact, the antenna performance of the metal tip improves with the tip material's conductivity, which for metals in the infrared increases monotonically with wavelength. Consequently, the s-SNOM can be predicted to function even better in the long-wavelength or terahertz spectral regions.

One unique capability of s-SNOM is the imaging of vibrational contrast, especially the mid-infrared 'fingerprint' spectra which can identify any material's chemical composition. This application has only barely been touched upon, mainly because the narrow tuning range of the CO_2 laser has not allowed us to deal with any strong polymer or biopolymer resonances (Lahrech *et al*. 1996; Knoll & Keilmann 1999*c*; Akhremitchev *et al*. 2001). In order to fully exploit this application, it will be necessary to introduce other infrared coherent light sources, as, for example, fixed-wavelength quantum cascade lasers (Faist *et al*. 1994) as we have already begun (Hillenbrand *et al*. 2002), or optical parametric oscillators, or wide-band coherent terahertz or mid-infrared radiation derived from femtosecond optical lasers (Auston & Cheung 1985; Bonvalet *et al*. 1995), or, finally, free-electron lasers.

The ability to do nanoscale microscopy in the infrared has a further, enormous application potential in solid-state physics, because many elementary excitation processes apart from vibrations or phonons lie at specific infrared frequencies. We have shown already that the conductivity of subsurface mobile carriers in Si can be probed by the infrared near field; the electron density has even been measured quantitatively (Knoll & Keilmann 2000*b*). Wavelength tuning could in addition determine the carrier mobility. A very interesting application of the s-SNOM's general ability to determine complex local conductivity on a nanoscale is to map conduction phenomena such as Cooper pairs in superconductors, potential modulation in carbon nanotubes or edge states in two-dimensional electron systems (Merz *et al*. 1993), and seems especially valuable when performed at the infrared wavelength matched, e.g. to Cooper pair breaking, plasmon-phonon coupling or cyclotron resonance, all of which constitute well-established elementary solid-state excitations not yet spectroscopically investigated on a nanoscale.

References

Adam, P.-M., Benrezzak, S., Bijeon, J. L. & Royer, P. 2000 Localized surface plasmons on nanometric gold particles observed with an apertureless scanning near-field optical microscope. *J. Appl. Phys.* **88**, 6919–6921.

Aigouy, L., Andreani, F. X., Boccara, A. C., Rivoal, J. C., Porto, J. A., Carminati, R., Greffet, J. J. & Megy, R. 2000 Near-field optical spectroscopy using an incoherent light source. *Appl. Phys. Lett.* **76**, 397–399.

Akhremitchev, B. B., Pollack, S. & Walker, G. C. 2001 Apertureless scanning near-field infrared microscopy of a rough polymeric surface. *Langmuir* **17**, 2774–2781.

Aravind, P. K. & Metiu, H. 1983 The effects of the interaction between resonances in the electromagnetic response of a sphere-plane structure; applications to surface enhanced spectroscopy. *Surf. Sci.* **124**, 506–528.

Auston, D. H. & Cheung, K. P. 1985 Coherent time-domain far-infrared spectroscopy. *J. Opt. Soc. Am.* B **2**, 606–612.

Azoulay, J., Debarre, A., Richard, A. & Tchenio, P. 2000 Optical contrast in apertureless microscopy. *Appl. Opt.* **39**, 129–134.

Betzig, E., Trautmann, J. K., Harris, T. D., Weiner, J. S. & Kostelak, R. L. 1991 Breaking the diffraction barrier: optical microscopy on a nanometric scale. *Science* **251**, 1468–1470.

Binnig, G. & Rohrer, H. 1982 Scanning tunneling microscopy. *Helv. Phys. Acta* **55**, 726–735.

Binnig, G., Quate, C. F. & Gerber, C. 1986 Atomic force microscopy. *Phys. Rev. Lett.* **56**, 930–933.

Bohren, C. F. & Huffmann, D. R. 1983 *Absorption and scattering of light by small particles.* Wiley-Interscience.

Bonvalet, A., Joffre, M., Martin, J. L. & Migus, A. 1995 Generation of ultrabroadband femtosecond pulses in the mid-infrared by optical rectification of 15 fs light pulses at 100 MHz repetition rate. *Appl. Phys. Lett.* **67**, 2907–2909.

Bragas, A. V. & Martinez, O. E. 2000 Field enhanced scanning optical microscope. *Opt. Lett.* **25**, 631–633.

Bridger, P. M. & McGill, T. C. 1999 Observation of nanometer-scale optical property discrimination by use of a near-field scanning apertureless microscope. *Opt. Lett.* **24**, 1005–1007.

Faist, J., Capasso, F., Sivco, D. L., Sirtori, C., Hutchinson, A. L. & Cho, A. Y. 1994 Quantum cascade laser. *Science* **264**, 553–556.

Fischer, U. C. 1998 Latex projections patterns. In *Procedures in scanning probe microscopy* (ed. R. J. Colton, A. Engel, J. E. Frommeret *et al.*), pp. 10–11. Wiley.

Hartschuh, A., Sanchez, E. J., Xie, X. S. & Novotny, L. 2003 High-resolution near-field Raman microscopy of single-walled carbon nanotubes. *Phys. Rev. Lett.* **90**, 095503.

Hayazawa, N., Inouye, Y., Sekkat, Y. & Kawata, S. 2002 Near-field Raman imaging of organic molecules by an apertureless metallic probe scanning optical microscope. *J. Chem. Phys.* **117**, 1296–1301.

Hecht, B., Sick, B., Wild, U. P., Deckert, V., Zenobi, R., Martin, O. J. F. & Pohl, D. W. 2000 Scanning near-field optical microscopy with aperture probes: fundamentals and applications. *J. Chem. Phys.* **112**, 7761–7774.

Hillenbrand, R. 2001 Nahfeldoptische Amplituden- und Phasenkontrastmikroskopie zur nanoskopischen Abbildung von Materialkontrast und optisch resonanten Partikeln. Fakultät für Physik, Technische Universität, München.

Hillenbrand, R. & Keilmann, F. 2000 Complex optical constants on a subwavelength scale. *Phys. Rev. Lett.* **85**, 3029–3032.

Hillenbrand, R. & Keilmann, F. 2001 Optical oscillation modes of plasmon particles observed in direct space by phase-contrast near-field microscopy. *Appl. Phys.* B **73**, 239–243.

Hillenbrand, R. & Keilmann, F. 2002 Material-specific mapping of metal/semiconductor/dielectric nanosystems at 10 nm resolution by back-scattering near-field optical microscopy. *Appl. Phys. Lett.* **80**, 25.

Hillenbrand, R. & Keilmann, F. 2003 Coherent imaging of nanoscale plasmon pattern with a carbon nanotube optical probe. *Appl. Phys. Lett.* **83**, 368–370.

Hillenbrand, R., Keilmann, F. & Knoll, B. 2000*a* Optische Nahfeldmikroskopie. German DE 10035134.

Hillenbrand, R., Stark, M. & Guckenberger, R. 2000*b* Higher-harmonics generation in tapping-mode atomic-force microscopy: insights into the tip–sample interaction. *Appl. Phys. Lett.* **76**, 3478–3480.

Hillenbrand, R., Knoll, B. & Keilmann, F. 2001 Pure optical contrast in scattering-type scanning near-field optical microscopy. *J. Microsc.* **202**, 77–83.

Hillenbrand, R., Taubner, T. & Keilmann, F. 2002 Phonon-enhanced light-matter interaction at the nanometre scale. *Nature* **418**, 159–162.

Inouye, Y. & Kawata, S. 1994 Near-field scanning optical microscope with a metallic probe tip. *Opt. Lett.* **19**, 159–161.

Jackson, J. D. 1975 *Classical electrodynamics.* Wiley.

Kneipp, K., Wang, Y., Kneipp, H., Perelman, L. T., Itzkan, I., Dasari, R. R. & Feld, M. S. 1997 Single molecule detection using surface-enhanced Raman scattering (SERS). *Phys. Rev. Lett.* **78**, 1667–1670.

Knoll, B. 1999 *Abtastende Nahfeldmikroskopie mit Infrarot- und Mikrowellen.* Aachen: Shaker.

Knoll, B. & Keilmann, F. 1999*a* Electromagnetic fields in the cutoff regime of tapered metallic waveguides. *Opt. Commun.* **162**, 177–181.

Knoll, B. & Keilmann, F. 1999*b* Mid-infrared scanning near-field optical microscope resolves 30 nm. *J. Microsc.* **194**, 512–515.

Knoll, B. & Keilmann, F. 1999*c* Near-field probing of vibrational absorption for chemical microscopy. *Nature* **399**, 134–137.

Knoll, B. & Keilmann, F. 2000*a* Enhanced dielectric contrast in scattering-type scanning near-field optical microscopy. *Opt. Commun.* **182**, 321–328.

Knoll, B. & Keilmann, F. 2000*b* Infrared conductivity mapping for nanoelectronics. *Appl. Phys. Lett.* **77**, 3980–3982.

Koglin, J., Fischer, U. C. & Fuchs, H. 1997 Material contrast in scanning near-field optical microscopy at 1–10 nm resolution. *Phys. Rev. B* **55**, 7977–7984.

Kreibig, U. & Vollmer, M. 1995 *Optical properties of metal clusters.* Springer.

Krenn, J. R. (and 10 others) 1999 Squeezing the optical near-field zone by plasmon coupling of metallic nanoparticles. *Phys. Rev. Lett.* **82**, 2590–2593.

Krug, J. T., Sanchez, E. J. & Xie, X. S. 2002 Design of near-field optical probes with field enhancement by finite difference time domain electromagnetic simulation. *J. Appl. Phys.* **116**, 10 895–10 901.

Labardi, M., Patane, S. & Allegrini, M. 2000 Artifact-free near-field optical imaging by apertureless microscopy. *Appl. Phys. Lett.* **77**, 621–623.

Lahrech, A., Bachelot, R., Gleyzes, P. & Boccara, A. C. 1996 Infrared-reflection-mode near-field microscopy using an apertureless probe with a resolution of $\lambda/600$. *Opt. Lett.* **21**, 1315–1317.

Lewis, A., Isaacson, M., Harootunian, A. & Muray, A. 1984 Development of a 500 Å spatial resolution light microscope. *Ultramicroscopy* **13**, 227–232.

Merz, R., Keilmann, F., Haug, R. J. & Ploog, K. 1993 Nonequilibrium edge-state transport resolved by far-infrared microscopy. *Phys. Rev. Lett.* **70**, 651–653.

O'Keefe, J. L. 1956 Resolving power of visible light. *J. Opt. Soc. Am.* **46**, 359.

Pohl, D. W., Denk, S. & Lanz, M. 1984 Optical stethoscopy: image recording with resolution $\lambda/20$. *Appl. Phys. Lett.* **44**, 651–653.

Porto, J. A., Carminati, R. & Greffet, J. J. 2000 Theory of electromagnetic field imaging and spectroscopy in scanning near-field optical microscopy. *J. Appl. Phys.* **88**, 4845–4850.

Porto, J. A., Johannsson, P., Apell, S. P. & Lopez-Rios, T. 2003 Resonance shift effects in apertureless scanning near-field optical microscopy. *Phys. Rev. B* **67**, 085409.

Ruppin, R. J. 1982 Spherical and cylindrical surface polaritons in solids. In *Electromagnetic surface modes* (ed. A. D. Boardman), pp. 345–398. Wiley.

Salerno, M., Krenn, J. R., Lamprecht, B., Schnider, G., Ditlbacher, H., Felidj, N., Leitner, A. & Aussenegg, F. R. 2002 Plasmon polaritons in metal nanostructures: the optoelectronic route to nanotechnology. *Optoelectron. Rev.* **10**, 217–224.

Sasaki, Y. & Sasaki, H. 2000 Heterodyne detection for the extraction of the probe-scattering signal in scattering type scanning near-field optical microscope. *Jpn. J. Appl. Phys.* **39**, L231–L323.

Specht, M., Pedarnig, J. D., Heckl, W. M. & Hänsch, T. W. 1992 Scanning plasmon near-field microscopy. *Phys. Rev. Lett.* **68**, 476–479.

Stark, M., Stark, R. W., Heckl, W. M. & Guckenberger, R. 2002 Inverting dynamic force microscopy: from signals to time-resolved interaction forces. *Proc. Natl Acad. Sci. USA* **99**, 8473–8478.

Stöckle, R. M., Suh, Y. D., Deckert, V. & Zenobi, R. 2000 Nanoscale chemical analysis by tip-enhanced Raman spectroscopy. *Chem. Phys. Lett.* **318**, 131–136.

Taubner, T., Hillenbrand, R. & Keilmann, F. 2003 Performance of visible and mid-infrared scattering-type near-field optical microscopes. *J. Microsc.* **210**, 311–314.

Völcker, M., Krieger, W. & Walther, H. 1994 Laser-frequency mixing in a scanning force microscope and its application to detect local conductivity. *J. Vac. Sci. Technol.* B **12**, 2129–2132.

Wang, S. 1976 Antenna properties and operation of metal–barrier–metal devices in the infrared and visible regions. *Appl. Phys. Lett.* **28**, 303–305.

Wessel, J. 1985 Surface-enhanced optical microscopy. *J. Opt. Soc. Am.* **2**, 1538–1540.

Wickramasinghe, H. K. & Williams, C. C. 1990 Apertureless near field optical microscope. US Patent 4 947 034.

Wurtz, G., Bachelot, R. & Royer, P. 1998 A reflection-mode apertureless scanning near-field optical microscope developed from a commercial scanning probe microscope. *Rev. Scient. Instrum.* **69**, 1735–1743.

Xu, H., Bjerneld, E. J., Käll, M. & Börjesson, L. 1999 Spectroscopy of single hemoglobin molecules by surface enhanced Raman scattering. *Phys. Rev. Lett.* **83**, 4357–4360.

Zenhausern, F., Martin, Y. & Wickramasinghe, H. K. 1995 Scanning interferometric apertureless microscopy: optical imaging at 10 angstrom resolution. *Science* **269**, 1083–1085.